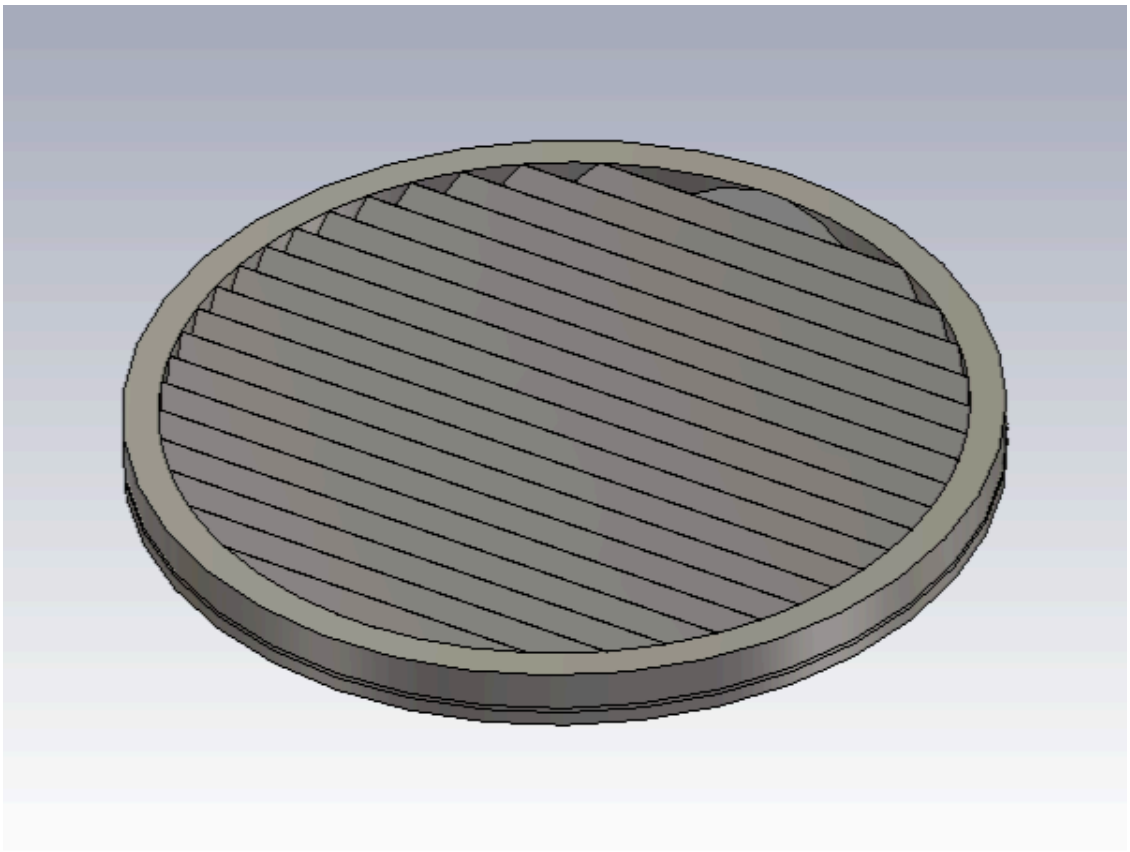

An 80 GHz Lens Fed CTS Array Antenna for Measurements on Solid Flows

Master's thesis in Wireless, Photonics and Space Engineering

Gustav Persson

DEPARTMENT OF ELECTRICAL ENGINEERING

CHALMERS UNIVERSITY OF TECHNOLOGY
Gothenburg, Sweden 2025
www.chalmers.se

Master's thesis 2025

An 80 GHz Lens Fed CTS Array Antenna for Measurements on Solid Flows

GUSTAV PERSSON

CHALMERS
UNIVERSITY OF TECHNOLOGY

Department of Electrical engineering
Chalmers University of Technology
Gothenburg, Sweden 2025

An 80 GHz Lens Fed CTS Array Antenna for Measurements on Solid Flows
GUSTAV PERSSON

Supervisor: Qiao Chen, Department of Electrical Engineering
Supervisor: Tasmiah Shaikh, Emerson
Examiner: Jian Yang, Department of Electrical Engineering

Master's Thesis 2025
Department of Electrical Engineering
Chalmers University of Technology
SE-412 96 Gothenburg
Telephone +46 31 772 1000

Cover image: Model of the designed Lens fed CTS array antenna

Typeset in LaTeX
Gothenburg, Sweden 2025

An 80 GHz Lens Fed CTS Array Antenna for Measurements on Solid Flows
GUSTAV PERSSON
Department of Electrical Engineering
Chalmers University of Technology

Abstract

By being able to monitor the particle dynamics of certain industrial processes, valuable infor- mation is given about the process. This is an important prerequisite to be able to ensure the quality of the product and to gain insight, which can help optimize the process. To be able to detect and characterize increasingly small particles, high-performance short-range radar (SRR) is widely used. This study details the design process of a Lens fed Continuous Transverse Stub (CTS) Array antenna, operating in the 77-81 GHz band. The intended application for the fin- ished antenna is to be able to conduct measurements within a circulating fluidized bed reactor (CFB), which is an essential component in a broad range of production processes. The de- signed antenna consists of two main parts: 1) the lens and 2) the CTS array antenna. The lens part uses a low profile, compact 2 layer spherical parallel plate waveguide (PPW), to collimate the beam and couple it to the top layer. From the top layer, the beam is then radiated using the CTS array antenna, consisting of 20 periodic slots, optimized to achieve a highly directive beam. The electromagnetic simulations performed demonstrate that the designed antenna achieves a directivity of 32.96 dBi, with an HPBW of 2.55 degrees in the H-plane and an aperture efficiency of 50of the existing concept, along with real-life testing, is needed before any real conclusion can be drawn as to its suitability within the intended application.

Keywords: Continuous Transverse Stub array antenna, Spherical Lens, Antenna array, Par- allel plate waveguide, Circulating Fluidized Bed reactor.

Acknowledgements

This masters thesis has been conducted for the company Emerson, which I would like to thank for this opportunity, along with all those who have supported me throughout this thesis. A special thanks must be directed to my Chalmers supervisor, Qiao Chen, for his support, feedback and continuous engagement. I also want to thank my Emerson supervisor Tasmiah Shaikh for her guidance, expertise and help to connect my work to real-life applications. In addition to this, I would like to thank all my colleagues at Emerson for including me, as well as my friends and family for their unwavering support during this journey.

Gustav Persson, Gothenburg, June 2025

Contents

1 Introduction

In this section, the background of the project is presented, along with a description of the main aim of the work.

1.1 Background

In several of today's industrial applications, it is essential to be able to monitor particle dynamics, in order to maintain quality and gain a better understanding of the process.

One such industry is the pharmaceutical industry, where non-interfering monitoring of the production process is crucial, in order to be able to guarantee the quality of the finished product. Factors like varying powder flow, varying powder density and particle aggregation within the particle transfer tube, can have a major impact on the final product. This makes continuous monitoring of the process important for quality assurance. One very viable solution to overcome these challenges is the implementation of submillimeter wave pulse Doppler radars. Experiments have shown that these have the ability to monitor factors such as particle velocity, particle distribution, and mass flow rate through the transfer tube. These readings can then in turn be used to evaluate the quality of the product in real-time [1].

The core advantages of using radars operating at high frequencies is that they can achieve high penetration depth into particle clouds and that they are less sensitive to contamination on the measurement port, when externally mounted. This makes them suitable for monitoring processes within multiple other industries, in addition to the pharmaceutical industry. One such industry is the plastics and polymers industry, within which the company Borealis is one of the leading producers of polyolefin [2]. Polyolefin is the largest class of organic thermoplastic polymers and includes some of the most widely used commodity plastics in the world, such as polyethylene (PE) and polypropylene (PP) [3]. The technology used by Borealis to produce polyethylene is called Borstar® PE 3G and is the third generation of this technology launched in 2013. This process includes a wide array of reactors, including a circulating fluidized bed reactor, whose environment is characterized by high pressure and high temperatures [4]. In these types of reactors, the use of high-frequency radar is highly appealing, as the desired measurements can be obtained without interfering with the process. This is an important prerequisite to be able to examine the often harsh process environment present in these reactors [5].

1.2 Aim

The aim of this thesis is to design and fabricate an antenna intended for use in a circulating fluidized bed reactor (CFB). The finished antenna should be able to perform measurements within such a reactor. Beyond this, the designed antenna must also fulfill certain requirements for it to be compatible for use in the intended application. The new system implemented should;

- Operate at 80 GHz with a 77–81 GHz bandwidth
- Have low loss
- Have low back-reflection
- Have high beam quality
- Have a beamwidth of 3°
- Be able to fit within a 3 inch aperture

- Be able to withstand up to 150° C
- Be able to withstand up to 60 Bar of pressure
- Have a process seal fabricated from a sustainable and PFAS-free material

2 Theory

2.1 Circulating fluidized bed reactor

A circulating fluidized bed reactor, also known as a CFB reactor, is a type of reactor that suspends solid particles using a high-velocity fluid. The two main components of the CFB reactor is a riser and a solids return leg. A schematic drawing of a CFB reactor can be seen in Figure 1a. The riser is continuously fed with solids that are then carried upward through the riser using a high-velocity fluid, fluidizing the particles in the process. At the top of the riser, the mix then enters the solids return leg, where entrained solids are captured in a fluid-solid separator. Undesirable solids are then returned to the bottom of the riser, typically via a downcomer. The riser and the return loop, thus ultimately form a circulating loop which characterizes a CFB [6].

There are a large number of industrial applications of CFB technology. For instance, it is used in industries involving petroleum, chemical engineering and biotechnology [7]. CFB reactors are also used in the production of polyethylene (PE). An example of this is the Borstar® PE 3G process. A simplified process flow diagram, describing the general process, is shown in Figure 1b. The process starts in the prepolymerization reactor, where a catalyst and propane diluent are mixed with a number of chemicals. The slurry produced from this reactor is then sent to a loop reactor, where lower molecular weight and high density polymers are produced. In the flash tank, the diluent and unreacted components are then separated from the polymer, before entering the Gas Phase Reactor. Here, the polymer undergoes further polymerization, typically producing high molecular weight polymers, which in turn broadens the molecular weight distribution, adding strength to the material. After removal of unwanted residuals, the polymer powder is transferred to extrusion [4].

The difference in molecular weight during the different stages of the process also means that the particles have varying mean particle size. This, in turn, has a major effect on the antenna requirements. For instance, a smaller particle size means that a higher resolution is required to be able to distinguish the particles [8].

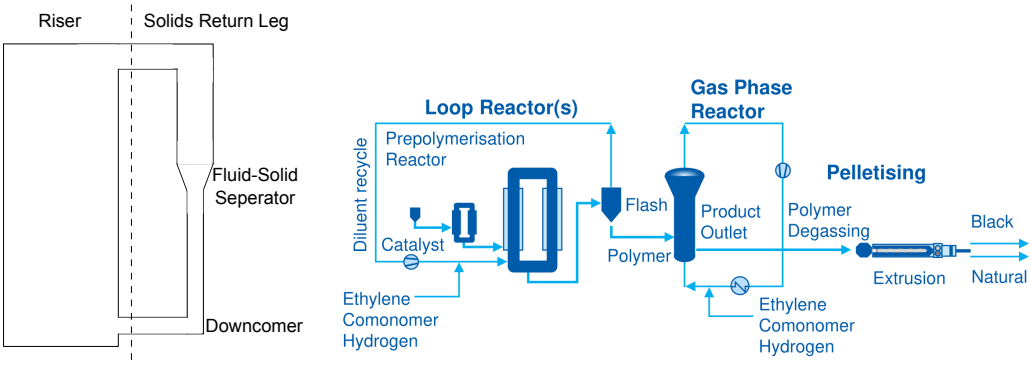

(a) Schematic of a CFB reactor **(b)** Simplified process flow diagram of the Borstar process [4].

2.2 Parallel plate waveguide

Understanding the operating principle of the parallel plate waveguide (PPW) is of great importance to understand the design choices made in this project. A PPW is a structure that is used to guide electromagnetic waves. The waves propagate through the waveguide using two plates.

These plates are conductors, which reflect the traveling wave between them. The distance between the plates determines the frequencies and modes that can propagate through it. The lowest frequency that can propagate is called the cutoff frequency.

The geometry of the PPW is shown in Figure 2. The plates are separated by a distance *d*, and the width of the plates are described by *W*. The width of the plates is assumed to be much larger than the separation of the plates, making it possible to effectively ignore fringing fields at the edges of the plate. Fringing fields basically mean that the fields start to curve outward instead of staying vertical and perpendicular to the plates. The region between the two plates is filled with a material with permittivity ε and permeability μ [9].

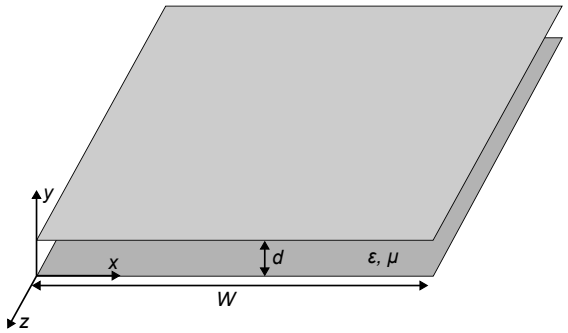

Figure 2: Geometry of a PPW.

There are three types of modes which can exist in a waveguide. These are the transverse electromagnetic (TEM), the transverse electric (TE) and the transverse magnetic (TM) modes. They are each named after how the electric and magnetic fields are oriented in relation to the direction of propagation. The fundamental TEM mode has no cutoff frequency, which means that it propagates at all frequencies. However, when the frequency is increased, it may reach the cutoff frequency of other modes. These will then begin to propagate alongside the fundamental mode, which can lead to undesirable effects. It is therefore common practice to avoid the propagation of higher-order modes. The cutoff frequency of the TE and TM mode is described by Equation 1, where n is an integer that describes the number of half-wavelength field variations, the mode has, in the direction perpendicular to the direction propagation [9].

$$f_{c_n} = \frac{n}{2d\sqrt{\mu\varepsilon}} \tag{1}$$

2.3 The scattering matrix

When analyzing and evaluating the performance of a network, a useful approach is to examine the scattering matrix, the elements of which are also known as the S-parameters. The scattering matrix relates the incident voltage waves (V_N^+) to the reflected voltage waves (V_N^-). For a network with N number of ports, the scattering matrix can be calculated according to Equation 2 [9].

$$\begin{bmatrix} V_1^- \\ V_2^- \\ \vdots \\ V_N^- \end{bmatrix} = \begin{bmatrix} S_{11} & S_{12} & \cdots & S_{1N} \\ S_{21} & S_{22} & \cdots & S_{2N} \\ \vdots & \vdots & \ddots & \vdots \\ S_{N1} & S_{N2} & \cdots & S_{NN} \end{bmatrix} \begin{bmatrix} V_1^+ \\ V_2^+ \\ \vdots \\ V_N^+ \end{bmatrix} \tag{2}$$

This means that an arbitrary element of the scattering matrix S_{ij} corresponds to the ratio of voltage reflected from the port i (V_i^-) in relation to the voltage incident on port j (V_j^+), as shown in Equation 3. For this to be applicable, all other ports except port j need to be terminated with a matched load, so that the incident wave on these ports is zero ($V_k^+ = 0$) [9].

$$S_{ij} = \left. \frac{V_i^-}{V_j^+} \right|_{V_k^+ = 0 \text{ for } k \neq j} \tag{3}$$

If a 2-port system is considered, $|S_{11}|$ would correspond to the reflection coefficient at port 1 - that is, the portion of the signal incident on port 1 that is reflected back to port 1. In the same way $|S_{21}|$ would correspond to the transmission coefficient from port 1 to port 2. In other words, the portion of the signal incident on port 1 that is transmitted to port 2. Similarly, $|S_{22}|$ would correspond to the reflection coefficient at port 2 and $|S_{12}|$ to the transmission coefficient from port 2 to port 1. Since power is proportional to the square of the voltage, the power ratio between two ports can be determined by squaring the magnitude of the corresponding S parameter. For instance, the fraction of incident power at port 1, which is reflected back to port 1, is given by $|S_{11}|^2$.

2.4 Fundamental antenna concepts

To fully understand how antenna performance is measured and evaluated, a few key concepts are needed.

The first important concept is directivity, which basically describes the ratio of the intensity of the antenna radiation in a specific direction, relative to the average radiation in all directions [10]. A highly directive beam thus means that a large portion of the radiation is being directed in a certain direction. Directivity is conventionally plotted w.r.t. the direction of the main beam and through this another important concept can be introduced. At a point of 3 dB under the main lobe peak, the 3dB-beamwidth, also known as the half-power beamwidth (HPBW), can be measured. This corresponds to the angle between two points on either side of the main lobe, where the radiation intensity has dropped to half of its maximum value. This value is a highly useful indicator of how well focused the main beam is [11]. An example of a normalized directivity plot with the HPBW marked, can be seen in Figure 3.

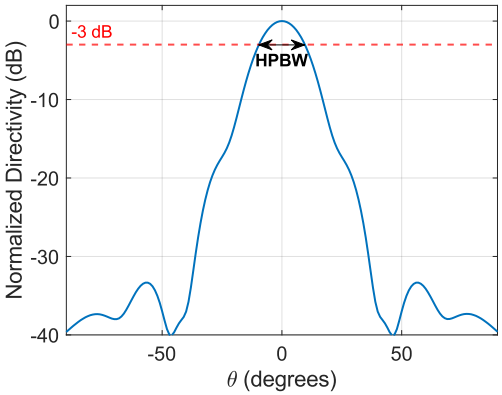

Figure 3: Example of a Directivity plot with the HPBW marked.

A highly directive or focused beam is achieved by collimating the beam. A beam is referred to as collimated when the rays are parallel, traveling in the same direction and deviate minimally as they propagate. A collimated beam is visualized in Figure 4a. There are numerous ways to collimate a beam. This can for instance be done using a collimator, such as a spherical lens which is shown in Figure 4b. In this case, the spherical mirror effectively transforms a spherical wavefront, emerging from the focal point, into a planar wavefront through reflection [12].

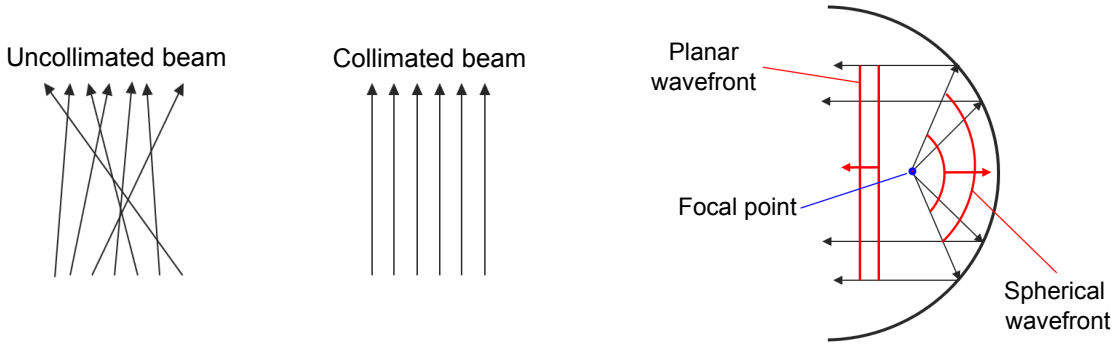

(a) Collimated and Uncollimated beam.

(b) Spherical mirror used to collimate beam

2.5 Field regions

When an antenna radiates an electromagnetic field, its behavior will change with increasing distance. To model this change, the radiated field is often divided into field regions. Specifically, the near-field region and the far-field region. The near-field region is, in turn, divided into an inner reactive near-field region and an outer radiating near-field region [11]. The field regions are illustrated in Figure 5.

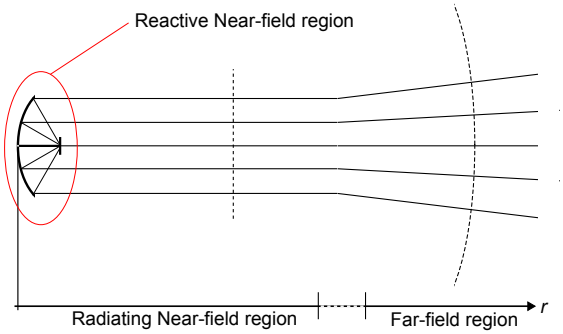

Figure 5: The field regions of an antenna.

Starting from the antenna itself, the field is initially characterized by the inner reactive near-field region. This small region closest to the antenna is defined by reactive and non-radiating fields dominating. The extent of the region is highly dependent on the geometry of the antenna. With increasing distance from the antenna, the field will then be characterized by the outer

radiative near-field region. Here, the radiating fields start dominating, but reactive fields are still present.

When the distance r from the antenna increases further, the far-field starts to form. At this point, the fields no longer vary with distance. It is common practice to state that the far-field has appeared when Equation 4 is fulfilled. In the formula, D corresponds to the diameter of the smallest possible sphere, which fits all the antenna components [11].

$$r \geq \frac{2D^2}{\lambda} \tag{4}$$

The field in the far-field region is generally considered to correspond to the radiation field of the antenna. Hence, studying the far-field is useful for determining and evaluating the final radiation pattern of the antenna [11]. This fact is highly useful and was used throughout the project to evaluate how changes in the design affected the radiation pattern.

2.6 Array theory

Single radiating elements often have a relatively wide radiation pattern, resulting in low directivity. However, in many applications, high gain and hence high directivity is of great importance for the antenna to work as intended. To achieve this, the electrical size of the antenna must be increased. There are multiple ways to accomplish this. One approach is to increase the size of the single radiating element. Another more effective approach is to form an assembly of radiating elements, without necessarily changing the size of the elements. The antenna formed by this assembly of elements is known as an array antenna. In order for the array to achieve a directive radiation pattern, the fields of the elements of the array need to interfere constructively in the desired direction while interfering destructively in all other directions. The geometry of a linear array, where N is the number of elements placed along a straight line, is shown in 6.

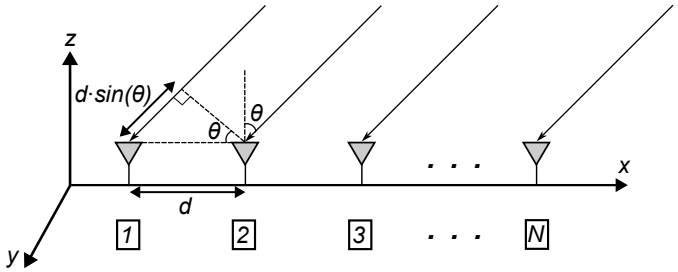

Figure 6: A N-element linear array.

If the elements of a linear array have isotropic radiation patterns, which means that they radiate equally in all directions, the overall radiation pattern of the array can be described by the array factor, AF. The array factor of a linear array is given by Equation 5 [10].

$$\begin{cases} AF(\theta,\phi) = \sum_{n=1}^{N} a_n e^{j(n-1)(kd\sin(\theta)+\phi)} \\ k = \frac{2\pi}{\lambda} \end{cases} \tag{5}$$

In the equation, a_n corresponds to the element amplitude, N to the number of elements, θ to the angle between the array axis and the observation direction, ϕ to the phase shifts between the elements, d to the element spacing and k to the wavenumber. Given the amplitude distribution across the elements, this equation makes it possible to evaluate the radiation pattern of a linear

array of isotropic radiators. The amplitude distribution has a considerable effect on the array factor and hence the radiation pattern of the linear array. To visualize this, the array factor was calculated for two different amplitude distributions, as shown in Figure 7. In these calculations 20 elements with element spacing λ were considered, at 80 GHz. The uniform distribution was obtained, using a constant amplitude distribution across the slots, while the Taylor distribution was obtained using the function `taylorwin()` in MATLAB [13].

As seen in Figure 7b, the uniform amplitude distribution results in a highly directive main beam, but relatively high sidelobe levels. The array factor in Figure 7d, illustrates that the Taylor distribution results in lower sidelobe levels at the expense of the directivity of the main beam. In both cases grating lobes can be observed at ± 90 degrees. This is due to the periodicity of the sine function. The grating lobes appear when $d\sin(\theta) = p\lambda$ where $p = \pm 1, \pm 2,....$ For a spacing of λ, this corresponds to ± 90 degrees [11].

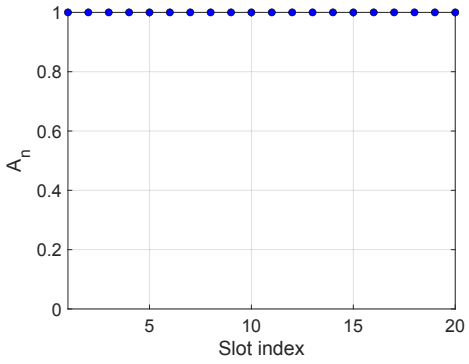

(a) Uniform amplitude distribution.

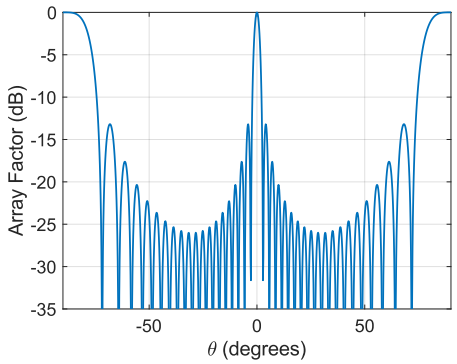

(b) Array factor using uniform amplitude distribution.

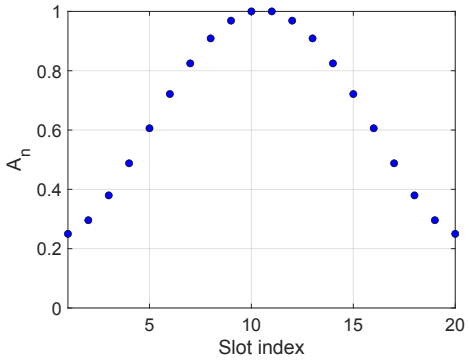

(c) Taylor amplitude distribution.

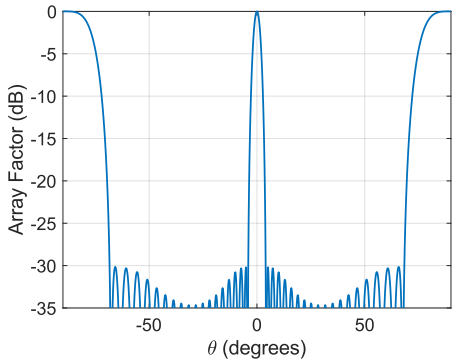

(d) Array factor using Taylor amplitude distribution.

Figure 7: Amplitude distributions and their corresponding array factor.

In general, the elements of an array do not exhibit isotropic radiation patterns. Because of this, the array factor will generally not represent the radiation pattern of an array. However, the radiation pattern of the complete array can be obtained by multiplying the radiation pattern of a single element, by the array factor, as shown in Equation 6 [10].

$$E_{tot}(\theta,\phi) = E_{element}(\theta,\phi) \cdot AF(\theta,\phi) \tag{6}$$

Thus, by optimizing the radiation pattern of a single element, which is also known as the element pattern, one can effectively suppress the grating lobes present in the array factor. This fact is highly useful when optimizing the radiation pattern of a linear array, such as a continuous transverse stub array.

3 Method

In this section, the different design steps are described in detail. First, the proposed antenna concept is presented. The design process of the lens and Continuous transverse stub (CTS) array antenna is then described in detail and finally combined, creating the Lens fed Continuous Transverse Stub array Antenna. To be able to evaluate the performance of the different antenna components, simulations were carried out in the 3D EM analysis software tools CST Studio Suite [14] and ANSYS HFSS [15].

3.1 Concept

The antenna designed in this project was based on a novel design, consisting mainly of two parts. Specifically a lens and a CTS array antenna. The purpose of the lens is to collimate the beam while the CTS array antenna's purpose is to radiate the beam. The antenna was designed at an operating frequency of $f_0 = 80$ GHz. A simplified conceptual sketch of the proposed antenna is shown in Figure 8.

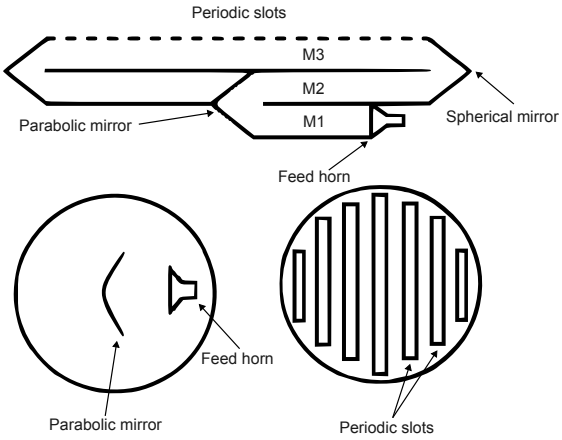

Figure 8: Antenna concept.

Starting from the first layer (M1), the wavefronts are excited by a feed horn. These then propagate through the first layer before being reflected up into the second layer by the first parabolic mirror. This parabolic mirror, which stretches between the first layer (M1) and the second layer (M2) of the lens, has a shape optimized to collimate the beam. The beam is then coupled to the third layer (M3) by the second spherical mirror, stretching between the second layer (M2) and the third layer (M3). The collimated beam emerging here is then radiated out through periodic slots placed in the top of the waveguide.

3.2 Lens design

3.2.1 Mirror design

The first part of the antenna designed was the mirror. Its main purpose is to efficiently transfer power between the different layers of the lens. The structure was modeled in CST, using perfect electric conductor (PEC) material. Since the mirrors used were going to be relatively wide in relation to the height of the mirror layers, it was deemed appropriate to simulate an infinitely

wide mirror. Therefore, a perfectly conducting magnetic boundary (PMC) was used on the faces of both mirror profiles (see Figure 9a). By inserting this boundary, the E-fields were kept parallel to the boundaries, while the H-fields were kept normal to the boundary. Hence, the electric field was kept continuous at the boundary while the magnetic field was mirrored at the boundary. This effectively simulated an infinitely wide mirror, which significantly reduced the simulation time in contrast to simulating a very wide mirror.

The height of both layers, denoted as h_{ppw} was chosen to be 0.9375 mm, which corresponds to a quarter of the wavelength in free space ($\lambda_0/4$), at the operating frequency. This dimension was chosen to avoid the excitation of higher-order modes and therefore ensure single-mode propagation of the fundamental TEM mode. Using Equation 1, the cutoff frequency of the first higher-order modes (TM_1 and TE_1) was determined to be 160 GHz and hence suppressed in the intended operating range of 77 to 81 GHz. The width of the mirror was selected to be 2.54 mm, corresponding to the width of a standard WR10 waveguide [9]. By implementing a chamfer edge, a smoother and more gradual transition is achieved between the layers. The abrupt geometrical discontinuity would otherwise lead to unwanted reflections, and hence less energy being transferred in the desired direction.

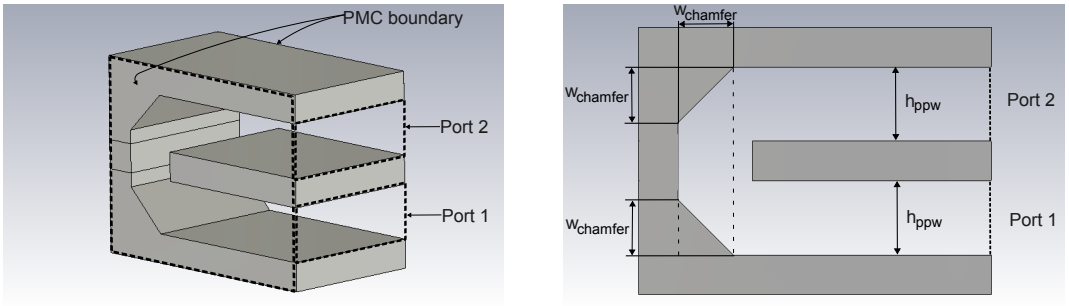

(a) 3D model view. **(b)** Mirror profile.

Figure 9: Geometry of mirror.

To maximize the energy being transferred from the bottom layer to the top layer, the reflections at port 1 needed to be minimized. To evaluate this, the reflection coefficient $|S_{11}|$ was measured, while performing a parametric sweep of the width of the chamfer, denoted as $W_{chamfer}$ in Figure 9b

The results of this study are visualized in Figure 10. The plot clearly demonstrates the importance of implementing a chamfer. Without a chamfer (that is, a chamfer width of 0 mm), the reflection coefficient at 80 GHz is −4.9 dB. From the plot it is clear that the chamfer width resulting in the least amount of reflections can be found between 0.6 and 0.8 mm. However, a chamfer width of 0.7 mm results in sufficiently low reflections. Therefore, further optimization was not deemed necessary and 0.7 mm was chosen as the chamfer width going forward.

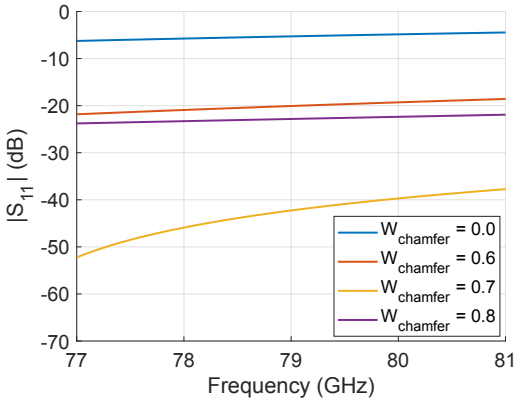

Figure 10: $|S_{11}|$ at different chamfer widths.

3.2.2 Pillbox lens design

The Pillbox lens was designed to assess the collimation of the beam. The structure, modeled in CST, consisted of two stacked circular PPWs, made of PEC, with the feed positioned in the bottom layer. The optimal mirror profile presented in Section 3.2.1, was implemented along the circumference of the lens to efficiently couple the beam to the top layer. The geometry of the Pillbox lens is presented in Figure 11.

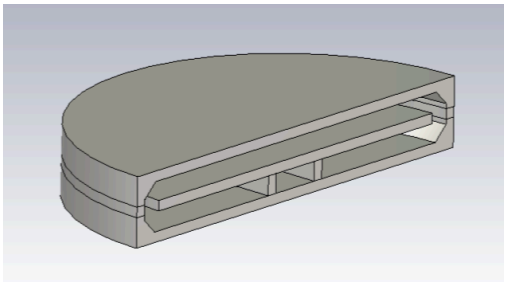

(a) 3D model view.

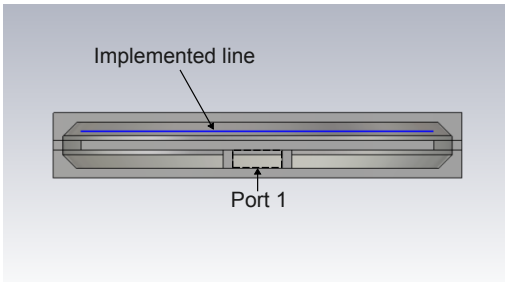

(b) Front view and implemented line.

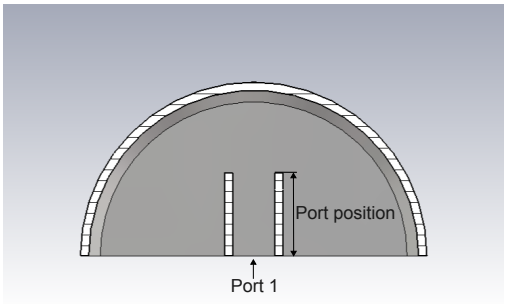

(c) Bottom layer.

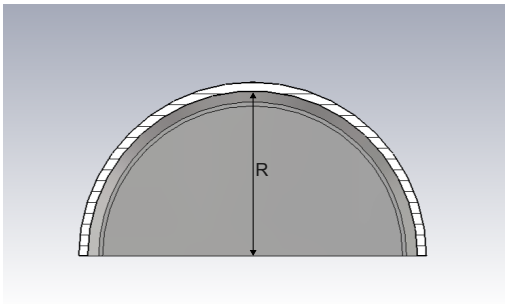

(d) Top layer.

Figure 11: Pillbox lens.

The height of both layers was set at 0.9375 mm ($\lambda_0/4$) to ensure single-mode propagation. The radius of the lens was arbitrarily chosen to be 10 mm to shorten the simulation time. For the feed, a width of 2.54 mm was used, corresponding to the width of a standard WR10 waveguide. As a starting point, the feed was placed at a 5 mm distance from the lens. This placement, which corresponds to the focal point of the lens, was chosen to achieve optimal beam collimation.

To evaluate the ability of the Pillbox lens to collimate the beam, the E-field was examined along an implemented line in the top layer. This line, shown in Figure 11b, was positioned on the flat edge of the lens and was vertically centered in the top layer. The length of this line was 18.125 mm, corresponding to the width of the middle plate. The primary focus when examining the E-field was on its phase and amplitude distribution, commonly referred to as the aperture distribution. As a starting point, a uniform feed was used. The position of the port was then varied, as shown in Figure 12a. This was done to investigate how the phase distribution could be improved. A parametric study was conducted, the results of which can be seen in Figure 12b. The plot illustrates that the smoothest and most consistent phase distribution can be found somewhere between 4 mm and 6 mm. Beyond this, it was observed that a very uniform phase distribution is achieved when the port is placed 5 mm from the lens edge. This corresponds to the focal point of the lens and confirms the previous assumption that this positioning would result in optimal beam collimation.

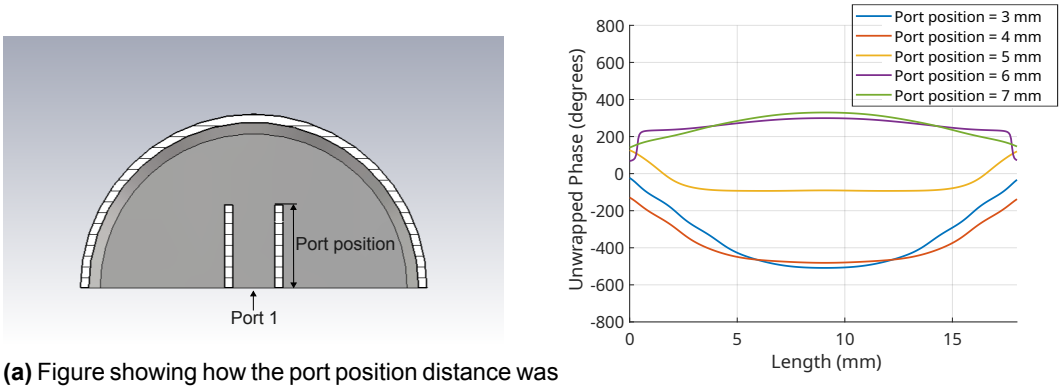

(a) Figure showing how the port position distance was varied.

(b) Phase distribution when varying port position.

Figure 12: Setup and result of the parametric study.

The feed was then replaced with the sectoral horn structure shown in Figure 13. The width of the narrow end of the horn, commonly known as the horn throat, was maintained at 2.54 mm as before. The opposite end, known as the horn aperture, was widened. The dimension of the widened end is hereafter referred to as Horn width. The horn was implemented to investigate how the amplitude distribution in the top layer could be improved. To evaluate this, the port position was held fixed at 5 mm, while a parametric study varying the horn width was conducted.

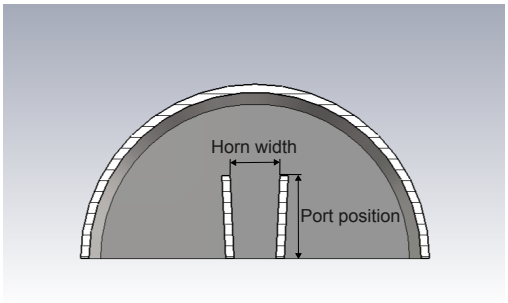

Figure 13: Figure showing how the horn width was varied.

The results of the parametric study are shown in Figure 14. Figure 14a illustrates the amplitude distribution along the implemented line and Figure 14b illustrates the phase distribution along the implemented line. Figure 14a demonstrates that an increasingly more tapered amplitude distribution is achieved when increasing the horn width. However, in Figure 14b it is also clear that the phase distribution becomes less uniform with increasing horn width. This is due to the phase center no longer being located in the focal point of the lens. When changing the geometry of the feed, the phase center is shifted. In a uniform feed, as shown in Figure 12a, the phase center is located at the aperture of the feed. This means that the focal point of the lens and the phase center coincide when the feed is placed half a radius from the lens. However, in a flared feed, such as a horn, the phase center is located behind the aperture, typically within the horn structure itself [16]. This leads to the phase center moving further away from the focal point with increasing horn width. This in turn leads to an increasingly less uniform phase distribution. The conclusion was therefore drawn that both the width and length need to be varied simultaneously to keep the phase center in the focal point of the lens.

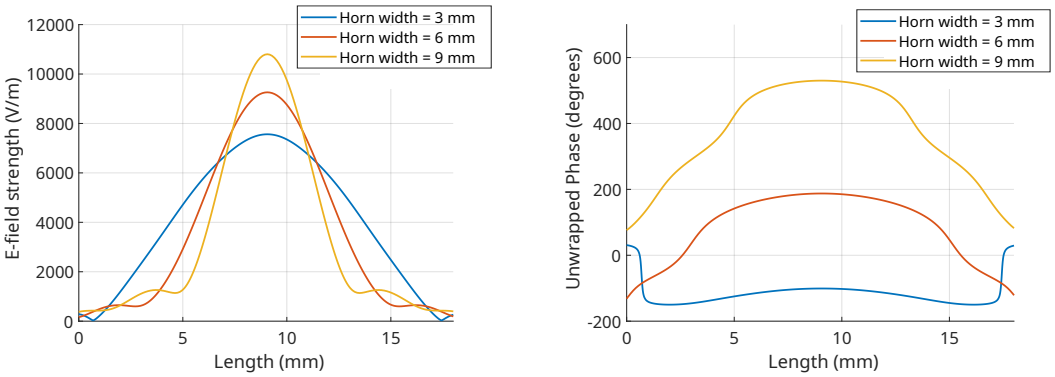

(a) Amplitude distribution when varying horn width. **(b)** Phase distribution when varying horn width.

Figure 14: Aperture distribution when varying horn width.

To show that a relatively uniform phase distribution can be achieved by varying both parameters, an optimization of the bottom layer feed was performed. This was realized using the built-in optimizer in CST. The objective of the optimization was to increase the uniform section of the phase distribution. To enable optimization, both the port position and the horn width were defined as variable parameters constrained within certain limits. The port position was allowed

to vary within a range of 4 to 6 mm, corresponding to a tolerance of $\pm$ 1 mm from the focal point of the lens. The horn width was constrained between 2.54 mm, corresponding to the dimension of the horn throat, and 5 mm, which corresponds to a value believed to be above the optimal.

In each of the parametric studies done so far, phase variations have appeared consistently, being especially prominent at the edges of the implemented curve. Therefore, it was concluded that the phase distribution will never be perfectly uniform across the entire length of the implemented line. When defining the optimizer goal, this had to be taken into account. The goal set was to minimize the phase deviation to $\pm$ 10 degrees. However, this is almost impossible to achieve along the entire implemented line. The goal was therefore limited to only apply to a new shorter 16 mm line. This line was positioned centered along the length of the previously implemented line in Figure 11b. A phase deviation of $\pm$ 10 degrees was considered acceptable because it corresponds to a small physical path length difference. At 80 GHz, a 10 degree deviation corresponds to a path length error of 0.1 mm, according to Equation 7. This value is very small compared to the wavelength and was therefore deemed to have a negligible impact on beam collimation and therefore an acceptable deviation.

$$\Delta L = \lambda \frac{\Delta\theta}{360^\circ} \tag{7}$$

The optimizer performed iterative simulations, adjusting the dimension of the variables in each iteration. This resulted in the following optimized parameters.

$$\begin{cases} \text{Horn width: } 2.98 \text{ mm} \\ \text{Port position: } 5.34 \text{ mm} \end{cases}$$

The aperture distribution of the Pillbox lens, when using the optimized parameters, is shown in Figure 15. Figure 15a shows that a slightly more tapered amplitude distribution has been achieved, compared to using a uniform feed. As seen in Figure 15b, the uniform portion of the phase distribution has been expanded at the expense of a somewhat less uniform distribution. Using the section of the phase distribution considered uniform (shown by the red lines in Figure 15b), the aperture effeciency can be approximated as the length of the uniform section over the entire aperture width. This results in an aperture efficiency of 14/20$\approx$70%.

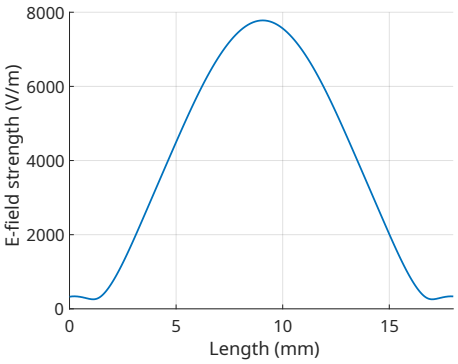

(a) Optimized amplitude distribution.

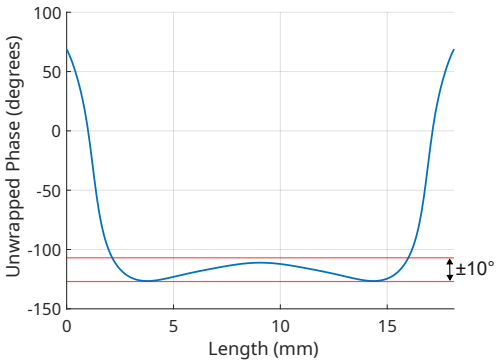

(b) Optimized phase distribution.

Figure 15: Optimized aperture distribution.

3.2.3 End-fire lens antenna design

The End-fire lens antenna was designed to assess the collimation of the beam, by investigating the far-field of the antenna. The structure is identical to the optimized Pillbox antenna presented in Section 3.2.2, differing only by the addition of a flare to the top layer. The flare was implemented to gradually transition the impedance of the top-layer PPW to that of free space, effectively reducing reflections at the aperture. The geometry of the End-fire lens antenna is presented in figure 16.

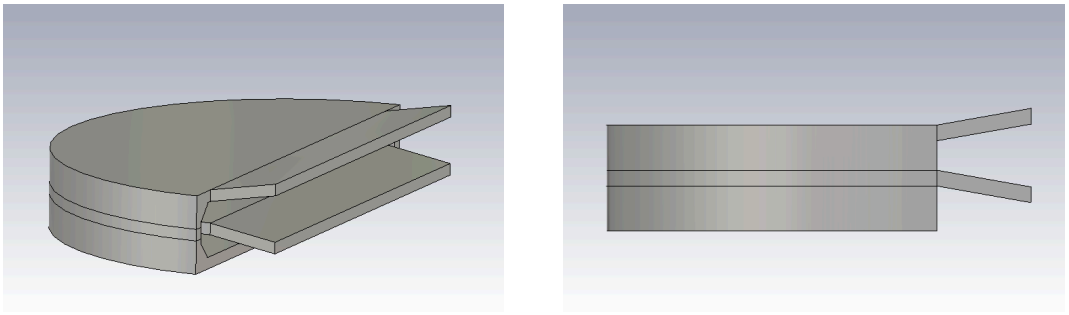

(a) 3D model view. **(b)** Side view.

Figure 16: End-fire lens antenna.

To speed up the optimization of the flare structure, it was designed separately. The structure consisted of two PEC plates with a linearly increasing separation toward the aperture. The width of the flare was selected to be 2.54 mm, corresponding to the width of a standard WR10 waveguide. A PMC boundary condition was used on the faces of the flare profile to effectively simulate a PPW. The initial height of the flare, h_{ppw}, was set to $\lambda/4$, corresponding to the height of the top layer of the Pillbox antenna. The parameters H and L were used to denote the height and length of the flare, respectively. The geometry of the flare is presented in Figure 17a.

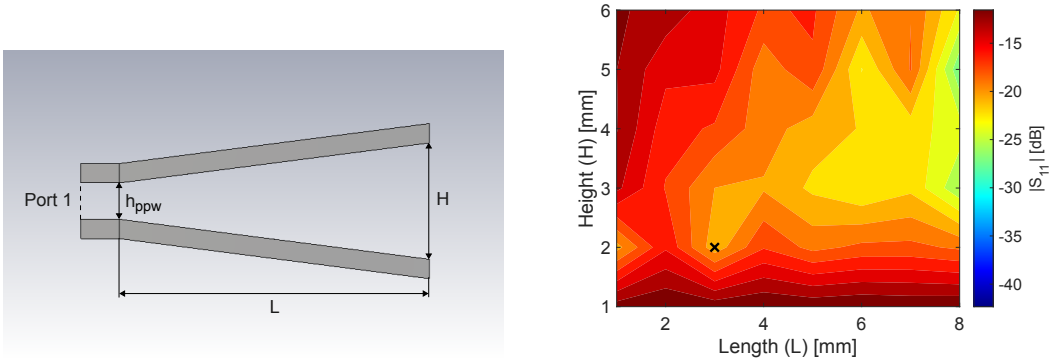

(a) Flare profile.

(b) Contour plot visualizing the variation in reflection coefficient $|S_{11}|$ at 80 GHz as a function of flare height H and length L. The selected configuration is marked with a black **x**.

Figure 17: Flare design.

To evaluate the ability of the flare to reduce reflections from free space, the reflection coefficient $|S_{11}|$ at port 1, was examined. A parametric study was conducted, varying the two parameters H and L. The results of this are visualized in Figure 17b, using a contour plot. The values shown for $|S_{11}|$ correspond to the magnitude measured at 80 GHz. The plot illustrates the effectiveness of the flare in reducing reflections when using an appropriate height-to-length ratio. At H=2 mm and L=3 mm the value of $|S_{11}|$ was -20.2 dB. This value was deemed sufficiently low for this application, as the flare will not be part of the final design. The configuration was therefore chosen to be used in the End-fire lens antenna. With the flare implemented, the far-field pattern of the antenna could now be studied. The simulated far-field pattern in the H-plane is shown in Figure 18b. The simulation result showed that the main lobe achieves a directivity of 13.8 dBi and an HPBW of 20.06 degrees, in the boresight direction.

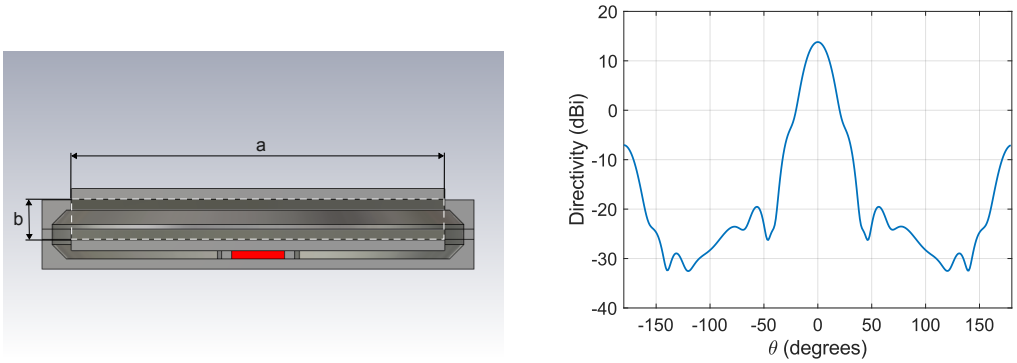

(a) Aperture area, marked with white dashed line. a= 18.125 mm and b= 2 mm

(b) Radiation pattern in the H-plane ($\phi = 0$).

Figure 18: Aperture and its radiation pattern.

This could now be used to calculate the simulated aperture efficiency of the End-fire lens antenna. To do this, the theoretical maximum directivity first needed to be calculated. This was done using Equation 8, where A_{ap} is the aperture area [11]. The aperture area is visualized in Figure 18a.

$$D_{max} = \frac{4\pi}{\lambda^2} \cdot A_{ap} \tag{8}$$

The theoretical maximum directivity, D_{max}, was calculated to be 15.1 dBi. This value could then be compared to the simulated directivity, D_0, of 13.8 dBi, resulting in the aperture efficiency as shown in Equation 9 [11].

$$e_{ap} = \frac{D_0}{D_{max}} \tag{9}$$

An aperture efficiency of 100% corresponds to a uniform aperture distribution [11]. The aperture efficiency can hence be used to evaluate how well collimated the beam is, since a lower aperture efficiency indicates phase or amplitude tapering across the aperture. The aperture efficiency, calculated using Equation 9, was found to be 66%, which is relatively high and therefore indicative of a well-collimated beam. However, it was deemed that this is the highest aperture efficiency achievable without implementing a secondary parabolic mirror.

3.3 Continuous transverse stub array antenna design

There are a wide range of techniques that can be used to generate and radiate highly directive beams. Previous implementations of the continuous transverse stub (CTS) array antenna have shown promising results in achieving a narrow beamwidth [17]. This approach of radiating the beam makes it possible to tailor the radiation pattern of the antenna, while also enabling future implementation of beam-steering.

3.3.1 Preliminary design calculations

The first step in designing the CTS array antenna was to determine the number of slots that would be needed to achieve the desired half-power beamwidth (θ_{3dB}) of 3 degrees. Using this requirement, the required directivity was estimated to be 36 dB, using Equation 10 [10].

$$D = \frac{4\pi}{(\theta_{3dB})^2} \tag{10}$$

The calculated directivity was then used to calculate the required aperture area, using Equation 11 [11].

$$D = \frac{4\pi}{\lambda^2} A_{ap} \implies A_{ap} = \frac{\lambda^2}{4\pi} D \tag{11}$$

The calculated area of 4420 mm^2, was then used to calculate the available space, for the slots. Since the aperture is circular, Equation 12, was used to calculate the diameter, along which the slots would be placed.

$$A_{ap} = \frac{\pi d^2}{4} \implies d = \sqrt{\frac{4A_{ap}}{\pi}} \tag{12}$$

The required diameter was calculated to be 75 mm, which is below the maximum allowed diameter (d_{max}) of 3 inches (76.2 mm), as described in Section 1.2. To ensure that each slot radiates at the same phase, the slot separation was chosen to be λ [17]. The number of slots able to fit on the aperture was then calculated to be 20, according to Equation 13.

$$N = \frac{d_{max}}{\lambda} \tag{13}$$

As described in Section 2.6, the amplitude distribution has a major effect on the final radiation pattern of the array. Since the final aim is a highly directive beam, a uniform amplitude distribution, shown in Figure 19a, was chosen in order to minimize the beamwidth. To visualize how the radiation pattern of such an array would look, assuming isotropic radiation, the array factor AF was calculated using the technique presented in Section 2.6. The result of this is shown in Figure 19b.

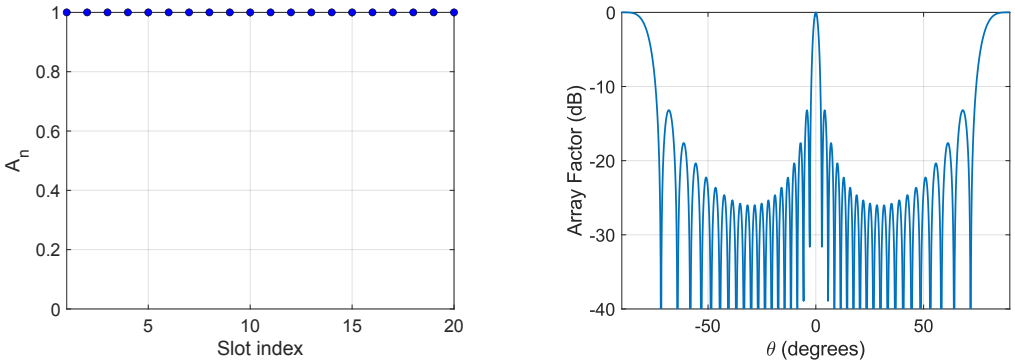

(a) Amplitude distribution. **(b)** Array factor.

Figure 19: Amplitude distribution and array factor of the target array.

Using a uniform amplitude distribution, the target power ratio, for each slot, can be calculated using Equation 14 [18]. This describes the ratio of the incoming power to each slot, that the slot needs to radiate in order to achieve the desired amplitude distribution.

$$P_{rad,i} = \frac{|A_i|^2}{\frac{1}{\eta}\sum_{i=1}^{N}|A_i|^2 - \sum_{i=1}^{N_i}|A_{i-1}|^2} \tag{14}$$

In this equation, A_i corresponds to the amplitude at slot index i and η corresponds to the target efficiency. N is the total number of slots and N_i is the number of the slot with index i. The resulting target power ratio, when using a uniform amplitude distribution and target efficiency $\eta = 0.99$, is shown in Figure 20

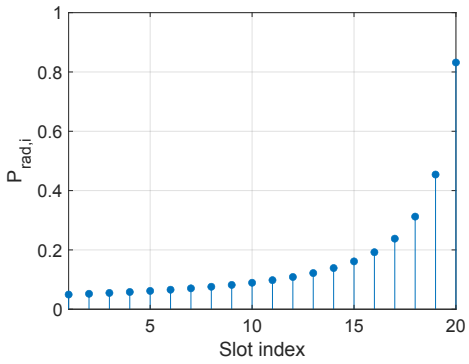

Figure 20: The target power ratio P_{rad} at each slot.

3.3.2 Unit cell design

The main purpose of the unit cell was to be able to optimize each slot to satisfy the required radiation ratio P_{rad} and to minimize $|S_{11}|$ and hence the reflections to port 1. The geometry of the designed unit cell is presented in Figure 21. The unit cell, designed in HFSS, consists of a

PEC-structure that models a PPW of height $\lambda_0/4$ and a radiating slot positioned above it. An airbox has also been placed on top of the radiating slot to enable far-field calculations. Beyond this a reflection canceling notch has been implemented in order to cancel out reflections from the radiating slot. Figure 21a, shows the parameters that were varied to evaluate their effect on P_{rad} and $|S_{11}|$.

The boundary conditions used for the unit cell are visualized in Figure 21b. The top side of the airbox has a radiation boundary condition, while the sides of the airbox uses two lattice pairs to simulate the mutual coupling between the radiating elements. PMC boundaries are used on the sides of the PEC-structure to effectively simulate an infinitely wide slot. Two ports are also implemented, enabling the extraction of the scattering parameters $|S_{11}|$ and $|S_{21}|$.

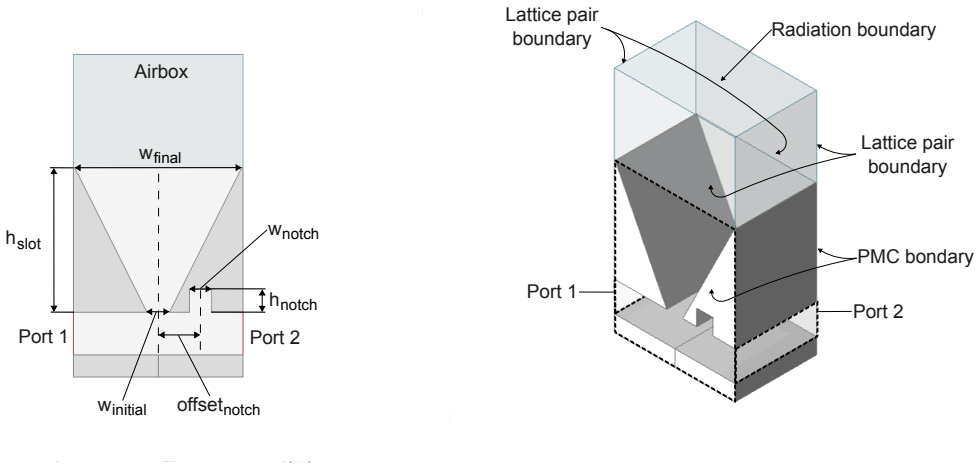

(a) Side profile of the unit cell.

(b) Boundaries of the unit cell.

Figure 21: The geometry of the designed unit cell.

In previous studies it has been shown that the simulated radiation ratio of a unit cell with two ports can be calculated according to the Equation 15 [19].

$$P_{rad} = 1 - |S_{11}|^2 - |S_{21}|^2 \tag{15}$$

The equation basically states that the power radiated through the slot can be equated to the incident power at port 1 subtracted by the power reflected back to port 1 and the power transmitted to port 2. This allows for the evaluation of how well the simulated radiation ratio of the unit cell, matches its target radiation ratio, shown in Figure 20.

As mentioned in Section 2.6, the element pattern describes the radiation pattern of the element. To suppress the grating lobes present in Figure 19b, the element pattern must be as directive as possible. The main parameter affecting this is the aperture width of the slot indicated as w_{final} in Figure 21a. To investigate the effect of the aperture width on the element pattern a parametric study was conducted. The results of this are shown in Figure 22. The plot shows that the element pattern becomes increasingly directive as the aperture width increases. The aperture width was therefore chosen to be 3.7 mm for all slots.

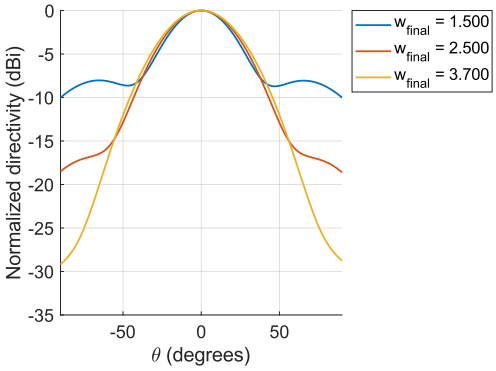

Figure 22: Element pattern of the unit cell at different aperture widths w_{final}.

The next step was to determine the height of the slot, denoted as h_{slot} in Figure 21a. The height of the slot was optimized to minimize the reflections at port 1. To evaluate this, a parametric study was conducted, the results of which can be seen in Figure 23. Based on this graph, h_{slot} was chosen to be 2.9 mm, as this dimension resulted in the lowest value of $|S_{11}|$ at the design frequency.

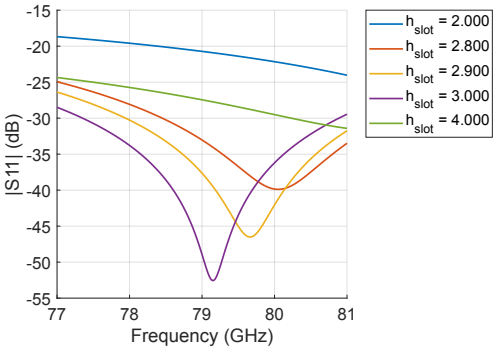

Figure 23: The reflection coefficient $|S_{11}|$ at different slot heights h_{slot}.

3.3.3 Array radiation pattern

There are multiple ways to obtain the radiation pattern of the array. The first method used was the one described previously in Section 2.6. This method entailed multiplying the element pattern with the array factor, according to Equation 6, to obtain the radiation pattern of the array. To realize this, the unit cell is shown in Figure 24a and its simulated element pattern, shown in Figure 24b, was used. By multiplying this and the array factor previously presented in Figure 19b, the radiation pattern of the array could be calculated, the result of which is shown in Figure 26, denoted as ”calculated”.

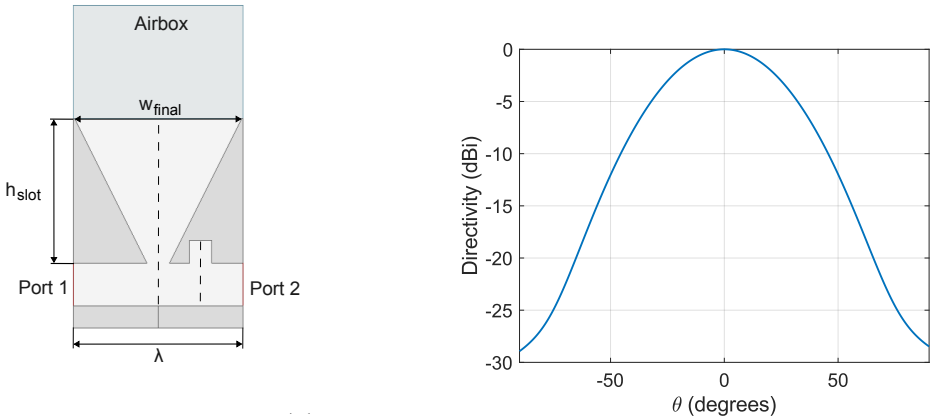

(a) Unit cell. **(b)** Element pattern.

Figure 24: Calculation - setup.

The radiation pattern was also simulated using HFSS, in order to take mutual coupling into account. This simulation used a modified unit cell, shown in Figure 25a. This unit cell is identical to the one presented in Figure 24a, except for the removed bottom section of the waveguide. The port has also been moved to the throat of the horn. The unit cell was simulated using the built-in array factor calculation method in HFSS, in order to obtain the radiation pattern of the array. 20 elements separated by a distance of λ and a uniform amplitude distribution were used. This simulation resulted in the ”simulated” radiation pattern shown in Figure 26.

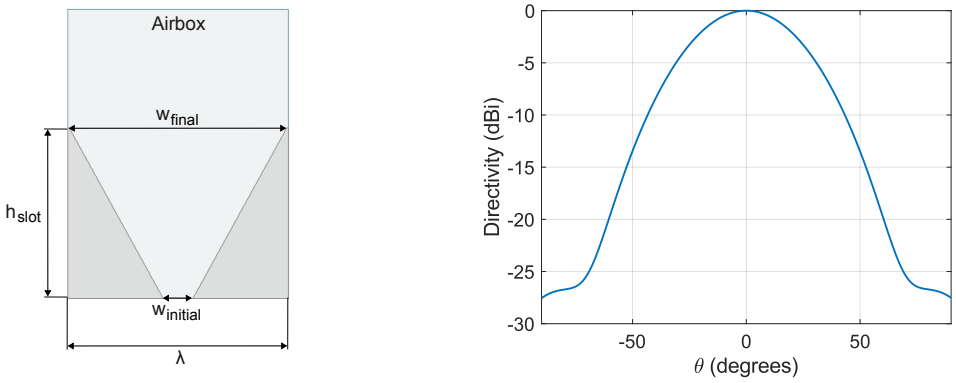

(a) Modified unit cell. **(b)** Element pattern.

Figure 25: Simulation - setup.

Overall, the two different approaches demonstrate a high level of conformity over the angular domain. The HPBW was evaluated to be 2.54 degrees using the calculation method and 3.02 degrees when using the simulation method. These results indicate that the goal of achieving a

3-degree HPBW is feasible. It is worth noting that both methods assume that all elements are identical, which will not be the case in the final array.

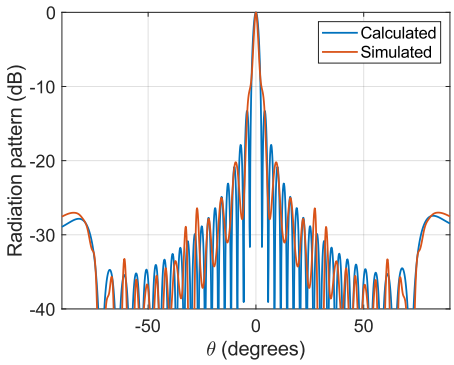

Figure 26: Calculated and simulated radiation pattern.

3.3.4 Linear array design

At this point, it was deemed necessary to conduct a series of parametric sweeps, in order to determine the remaining parameters which varies from slot to slot. The parameters swept were the initial slot width ($w_{initial}$), the offset of the notch ($offset_{notch}$), and the dimensions of the notch itself (w_{notch}) and (h_{notch}). The amount of power radiated through the slot was mainly controlled by the initial slot width ($w_{initial}$). The reflected wave was formed based on the dimensions of the notch, while the phase of the reflected wave was determined by the offset of the notch ($offset_{notch}$).

Once the parametric sweeps had been performed, the results were evaluated according to the goals set for the respective cell. The first goal for each unit cell was to achieve its respective target radiation ratio, with an accepted deviation of about 1% at the operating frequency. The second goal was to keep the reflection coefficient $|S_{11}|$ below -20 dB for every slot except for the last where a reflection coefficient of -10 dB was allowed. The reason for keeping the refection coefficient low overall is to avoid the reflected waves from accumulating and destructively interfering with the incident wave.

The parameter dimensions found for each slot can be seen in Figure 27. The resulting radiation ratio is compared to the target radiation ratio in Figure 28a and the reflection coefficient S_{11} is plotted for each slot in Figure 28b.

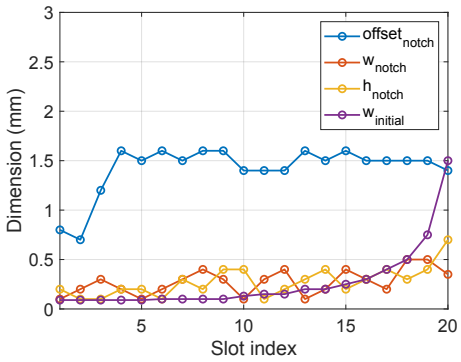

Figure 27: Paramater dimensions for each slot.

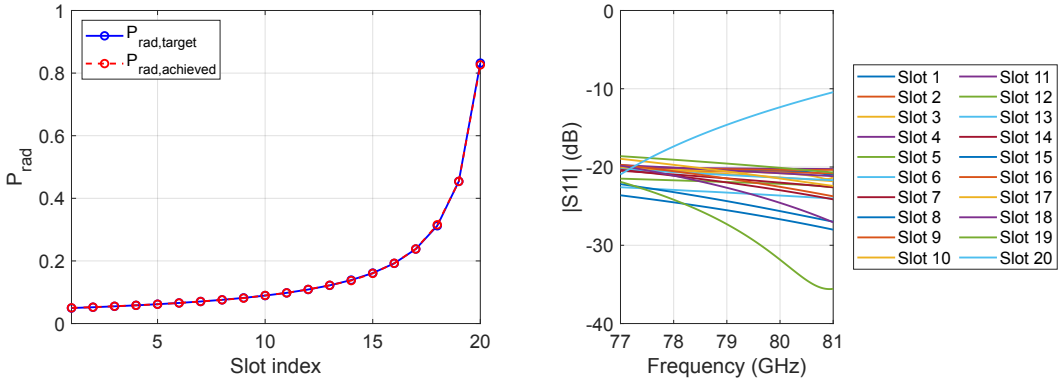

(a) Achieved radiation ratio compared to the target radiation ratio.

(b) Reflection coefficient.

Figure 28: Performance of the slots.

To assess the performance of the array, simulations were carried out in CST, after transferring the unit cells, from HFSS. The model used is shown in Figure 29. It consists of the 20 optimized unit cells cascaded to form the linear array. The structure width was arbitrary set to the width of a WR10 waveguide and PMC boundaries was used to simulate a PPW. 2 ports was also placed at each end of the array.

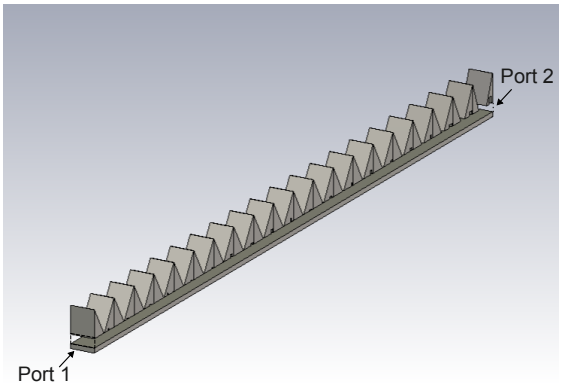

Figure 29: Geometry of the linear array.

In Figure 30 the simulation results of the linear array are presented. The HPBW is 2.48 degrees as shown in Figure 30a, thus fulfilling the requirement of keeping the beamwidth below 3 degrees. The aperture area of the linear array is 190.5 mm^2, corresponding to a theoretical maximum directivity of 22.3 dBi, according to Equation 8. The simulated directivity is 21.94 dBi, resulting in an aperture efficiency of 92 $\%$, according to Equation 9. The reflection coefficient for port 1 is plotted in Figure 30b and indicates that the reflection canceling notches might not be working optimally and could benefit from further optimization.

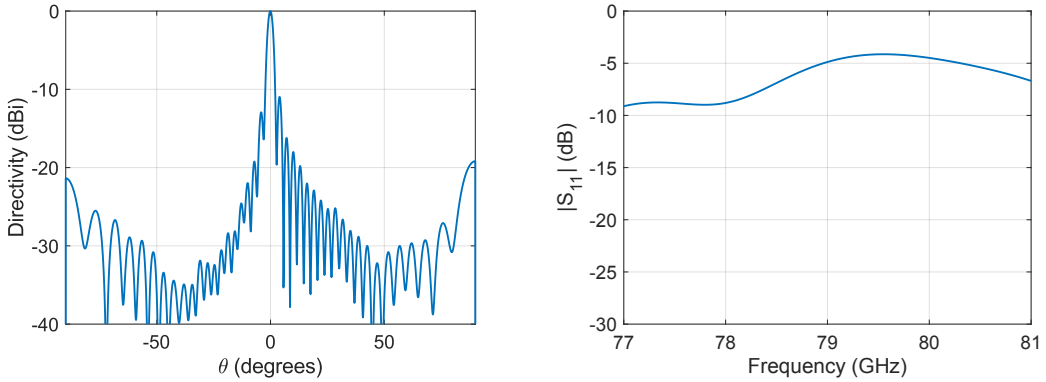

(a) Directivity in the H-plane.

(b) Reflection coefficient.

Figure 30: Performance of the slots.

3.4 Lens fed Continuous Transverse Stub Antenna

The last step of the design process was to combine the continuous transverse stub array antenna design and the lens design to create the Lens fed Continuous Transverse Stub Array Antenna, presented in Figure 31. The lens part consists of a circular 2 layer PPW. The height of both layers is set to $\lambda_0/4$. In the bottom layer, the feed is placed at the focal point of the lens, as shown in Figure 31d. The diameter d of the lens is 80 mm. The mirror designed in Section 3.2.1 was implemented along the circumference of the lens, to couple the power to the top layer, which is shown in Figure 31b. In the top layer, the slots designed in Section 3.3.4, are implemented in the upper conducting plate in the top layer of the PPW. The implemented slots are shown in Figure 31c. Here, the aperture area has been marked with a white dashed line. The aperture diameter d_{ap} is 75 mm, which corresponds to the width of 20 slots with λ spacing. This results in an aperture area A_{ap} of 4418 mm^2. The results of the CTS antenna are presented and discussed in Section 4.

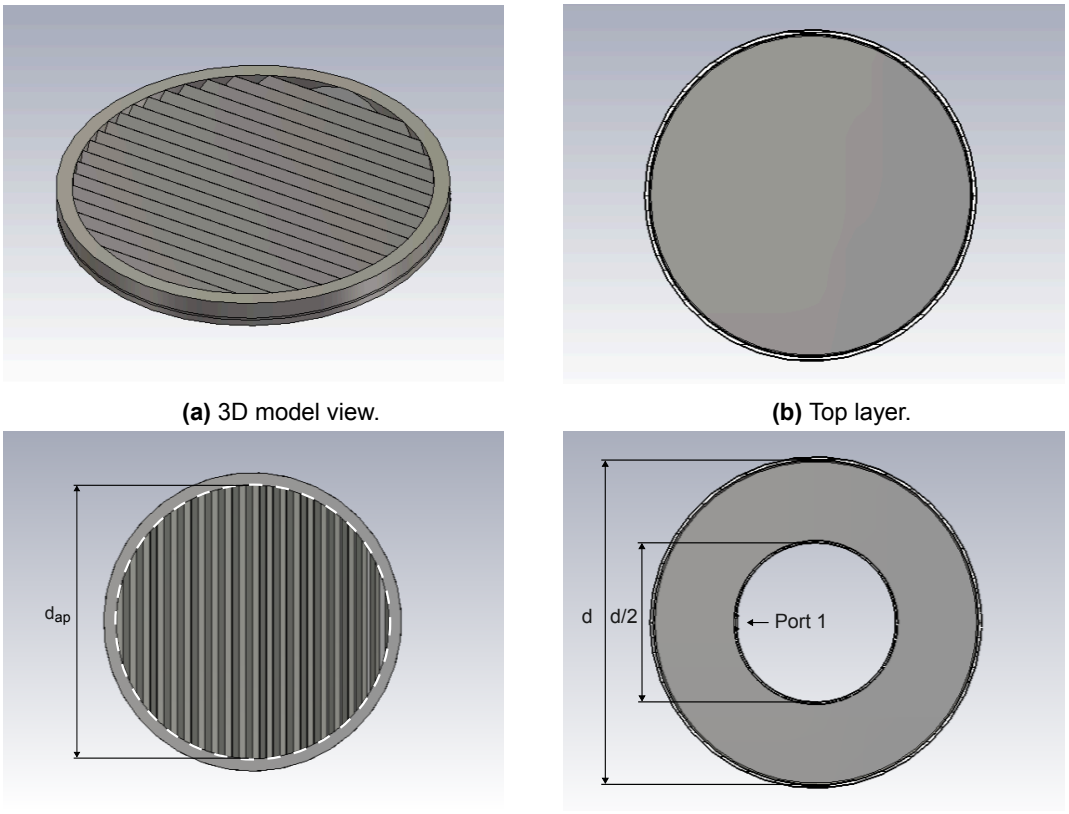

(a) 3D model view.

(b) Top layer.

(c) Top side.

(d) Bottom layer.

Figure 31: The geometry of the Lens fed CTS Antenna.

4 Results and discussion

In this section, the results of the Lens fed continuous transverse stub (CTS) array antenna is presented and discussed.

4.1 Radiation pattern

Figure 32 shows the simulated realized gain of the lens fed CTS array antenna at 80 GHz. The simulation shows good coherence with the expected array radiation pattern, calculated in Section 3.3.4. The main beam exhibits a HPBW of 2.55 degrees and 5.80 degrees, in the H-plane and E-plane respectively. Hence reaching the initial goal of a 3 degree HPBW in the H-plane, but not in the E-plane. This is mainly due to the lens part not completely collimating the beam. As seen in Sections 3.2.2 and 3.2.3, we typically obtain an aperture efficiency of about 70% using an optimized feed and the spherical mirror. To further improve the beamwidth in the E-plane, the aperture efficiency must be increased, which can be done through the implementation of the secondary parabolic mirror. Since a beamwidth narrower than the one required in the H-plane has been obtained, there is potential to simplify the design while still keeping the beamwidth below the specified requirement. This can be achieved by reducing the aperture size and thereby also reducing the number of slots. This would make the design more compact and would also likely simplify the fabrication process.

Both Figure 32a and Figure 32b clearly demonstrate the trade-off between beamwidth and side lobe levels (SLL). The H-plane with the narrower beamwidth exhibits a maximum SLL of -11.2 dB, while the E-plane with the wider beamwidth exhibits a maximum SLL of -20.78 dB.

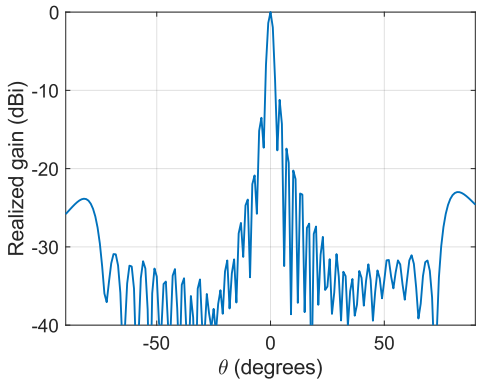

(a) H-plane ($\phi = 0$) at 80 GHz.

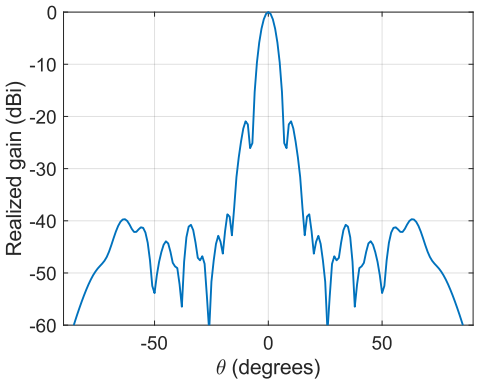

(b) E-plane ($\phi = 90$) at 80 GHz.

Figure 32: Simulated realized gain of the lens fed CTS array antenna.

The performance of the antenna was also evaluated by calculating the aperture efficiency. In Figure 33 the simulated 3D radiation pattern of the antenna is presented. At 80 GHz, the antenna exhibited a directivity of 32.96 dB. The theoretical maximum directivity of the aperture was calculated to be 35.96 dB. The aperture efficiency, evaluated using these values, was determined to be 50$\%$. This value is significantly lower than the simulated aperture efficiency of the linear array, presented in Section 3.3.4. This can also be explained by the lens part of the antenna failing to adequately collimate the beam, once again showing the significance of the parabolic mirror originally planned.

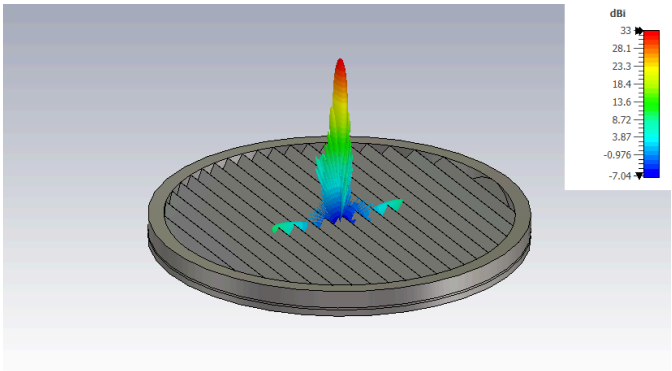

Figure 33: Simulated 3D radiation pattern of the lens fed CTS array antenna.

4.2 Reflections

Minimizing reflections within the antenna is essential to achieve favorable performance. Therefore, the reflection coefficient at the feed of the lens fed CTS array antenna was evaluated. The results of the simulation are shown in Figure 34 and confirms that the reflection canceling notches are not working properly. To achieve a lower reflection coefficient, the unit cells need to be further refined. The current unit cells have a requirement on the reflection coefficient being lower than -20 dB at Port 1 of the cell, as described in Section 3.3.4. To further reduce the reflections in the linear array, this requirement could be made stricter, by instead setting the requirement for the reflection coefficient to be below -30 dB. To find the optimal parameters that improve the reflection coefficient while maintaining the specified radiation ratio, more thorough parametric sweeps of the unit cell need to be conducted.

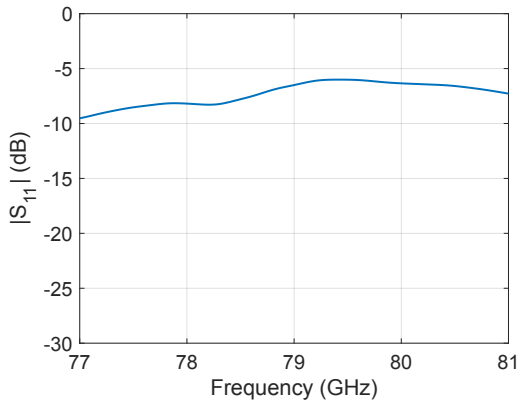

Figure 34: Simulated reflection coefficient of the lens fed CTS array antenna feed.

5 Conclusion and future work

In this section, the conclusions drawn from the project results are presented along with recommendations on future work.

5.1 Conclusion

The aim of the project was to design and fabricate an antenna intended for use in a circulating fluidized bed (CFB) reactor. The designed antenna demonstrates great potential to fulfill the given requirements. However, before any real conclusion can be drawn as to whether the designed antenna is suitable for the application, further optimization and development of the antenna is needed. Following the implementation of the necessary parts for the antenna to perform as intended, which are presented in Section 5.2, validation can be performed through real-life testing.

5.2 Future work

Due to the time limitation of this project, there were several aspects of the design that could not be realized. In this section, these are presented along with suggestions on how to continue the work.

5.2.1 Implementation of process seal

One of the initial requirements for the antenna was that it be fabricated of a sustainable and PFAS-free material. Although the antenna will be made mainly of metal, a protective layer will be necessary for the antenna to operate in the intended environment. This protective layer, known as a process seal, will shield the antenna from the harsh environment within the FBR. Regardless of which material is chosen to be used in the process seal, it will have an effect on the performance of the antenna, due to its different dielectric constant and loss tangent. This must be taken into account when implementing the seal.

In a previous master's thesis conducted for Emerson, alternative materials to PFAS have been evaluated. This study shows that while there are multiple viable alternatives to PFAS, achieving comparable performance generally entails a clear cost increase [20]. Due to its similarity to PFAS, PEEK is a strong contender to replace it. To investigate if it is suitable for this application, a short theoretical study was conducted. To evaluate its applicability, the compressive strength of the process seal was calculated. The contact area between the seal and its housing was first calculated using Equation 16 [21].

$$A_{seal} = \frac{\pi(d_{total}^2 - d_{aperture}^2)}{4} \tag{16}$$

Using a total diameter of 100 mm and the aperture diameter of 75 mm, the contact area was calculated to be 3436 mm^2. The force acting on the aperture area A_{ap}, subjected to a pressure of p, was then calculated using Equation 17 [21].

$$F = p \cdot A_{ap} \tag{17}$$

Using a circular aperture area with a diameter of 75 mm and the pressure requirement of 60 bar, it was found that the seal should be able to withstand approximately 20.6 kN of force.

These values were then used to calculate the needed compressive strength of the process seal, according to Equation 18 [22].

$$\sigma = \frac{F}{A_{seal}} \tag{18}$$

The required compressive strength was found to be 8.3 MPa. This value is well below the compressive strength of PEEK, which is 143.5 MPa. PEEK also meets the temperature requirement of being able to withstand 150° C, since it has a maximum continuous service temperature of 260° C [20].

5.2.2 Implementation of Parabolic mirror

As described in Section 3.1, the initial concept included a parabolic mirror, with a shape optimized to collimate the beam. The idea of implementing a parabolic mirror is to achieve better collimation than when using a spherical mirror. If the spherical mirror is implemented in the future, both the Pillbox design (see Section 3.2.2) and the End Fire Lens Antenna design (see Section 3.2.3), can be used to evaluate how well the spherical mirror collimates the beam.

Parabolic setups used to collimate beams have previously shown promising results. In [23], a pillbox transition was used to collimate the beam. The transition consisted of slots and vertical metallic pins placed in a parabolic pattern. The slots were used to couple the energy between the layers, while the pins acted as the parabolic reflector. By placing the feed in the focal point of the reflector, the spherical wavefront originating from the feed was transformed to a near planar wavefront, resulting in an average HPBW of 5.5° deg in the H-plane [23].

5.2.3 Higher frequencies

Part of the original plan was to also simulate a 340 GHz version of the designed antenna. Although there was not enough time to realize this version, it is deemed to be relatively easy to implement in the future. This is due to the scalability of the design, made possible by most of the antenna dimensions being directly dependent on the intended operating frequency.

References

[1] M. Bonmann, A. Moradikouchi, T. Bryllert, *et al.*, "Terahertz radar observes powder dynamics for pharmaceutical manufacturing," *IEEE Sensors Journal*, vol. 24, no. 13, pp. 20 512–20 522, 2024. DOI: 10.1109/JSEN.2024.3397399.

[2] Borealis Group, *About borealis*, Accessed: 2025-05-26, 2025. [Online]. Available: https://www.borealisgroup.com/about-us.

[3] S. Topics, *Polyolefin - an overview*, Accessed: 2025-05-26, 2023. [Online]. Available: https://www.sciencedirect.com/topics/materials-science/polyolefin.

[4] Borstar® PE 3G, *Borstar® pe 3g: Advanced polyethylene production process*, Accessed: 2025-05-26, 2025. [Online]. Available: https://portfolio-pplus.com/Technologies/Details/235.

[5] T. Bryllert, M. Bonmann, and J. Stake, "A submillimeter-wave fmcw pulse-doppler radar to characterize the dynamics of particle clouds," *IEEE Transactions on Terahertz Science and Technology*, vol. 13, no. 4, pp. 389–395, 2023. DOI: 10.1109/TTHZ.2023.3263641.

[6] C. Wang and J. (Zhu, "Circulating fluidized beds," in Apr. 2020, pp. 239–268, ISBN: 9783527340644. DOI: 10.1002/9783527699483.ch12.

[7] GEMCO Energy, *Applications of circulating fluidized bed technology*, https://gasificationplant.com/biomass-energy/applications-of-circulated-fluidized-bed-technology/, Accessed: 2025-06-09, 2024.

[8] W. G. Rees, *Physical Principles of Remote Sensing*, 3rd. Cambridge University Press, Dec. 2012, ISBN: 9780521181167. DOI: 10.1017/CBO9781139017411.

[9] D. M. Pozar, *Microwave Engineering*, 4th ed. Hoboken, NJ: Wiley, 2012, ISBN: 978-1-119-77061-9.

[10] C. A. Balanis, *Antenna Theory: Analysis and Design*, 3rd. Hoboken, NJ, USA: Wiley, 2005, Accessed: 2025-05-26. [Online]. Available: https://archive.org/details/Antenna.Theory.Analysis.and.Design3rd.Edition.

[11] P.-S. Kildal, *Foundations of Antenna Engineering: A Unified Approach for Line-of-Sight and Multipath*. Gothenburg, Sweden: Kildal Antenn AB, 2015, ISBN: 978-91-637-8515-3.

[12] B. E. A. Saleh and M. C. Teich, *Fundamentals of Photonics*, 3rd. Hoboken, NJ: Wiley, 2019, Part 1: Optics, ISBN: 9781119506867.

[13] T. M. Inc., *Taylorwin*, https://uk.mathworks.com/help/signal/ref/taylorwin.html, Accessed: 2025-05-28, Natick, Massachusetts, United States, 2025. [Online]. Available: https://uk.mathworks.com/help/signal/ref/taylorwin.html.

[14] SIMULIA, *Cst studio suite: Electromagnetic field simulation software*, Accessed: 2025-04-27. [Online]. Available: https://www.3ds.com/products/simulia/cst-studio-suite.

[15] Ansys Inc., *Ansys hfss: 3d electromagnetic field simulator for high-frequency and high-speed electronic components*, Version 2024 R2, 2024. [Online]. Available: https://www.ansys.com/products/electronics/ansys-hfss.

[16] J. Ruiz-García, E. Martini, C. D. Giovampaola, D. González-Ovejero, and S. Maci, "Reflecting luneburg lenses," *IEEE Transactions on Antennas and Propagation*, vol. 69, no. 7, pp. 3924–3935, 2021. DOI: 10.1109/TAP.2020.3044668.

[17] K. Tekkouk, J. Hirokawa, R. Sauleau, and M. Ando, "Wideband and large coverage continuous beam steering antenna in the 60-ghz band," *IEEE Transactions on Antennas and Propagation*, vol. 65, no. 9, pp. 4418–4426, 2017. DOI: 10.1109/TAP.2017.2723663.

[18] A. A. Oliner and D. R. Jackson, “Leaky-wave antennas,” in *Antenna Engineering Handbook*, J. L. Volakis, Ed., 4th, https://www.accessengineeringlibrary.com/content/book/9780071475747, McGraw-Hill Education, 2007, ch. 11.

[19] A. Ugle, “A travelling wave slot array based on a double-layer lens for 77 ghz automotive radar,” Accessed: 2025-05-30, Master’s thesis, KTH Royal Institute of Technology, Stockholm, Sweden, 2023. [Online]. Available: https://kth.diva-portal.org/smash/record.jsf?pid=diva2:1834156.

[20] L. Paronen, “Material selection for non-contacting radar process seal antenna,” English, Accessed: 2025-06-01, Master’s thesis, Lappeenranta-Lahti University of Technology (LUT), 2024. [Online]. Available: https://lutpub.lut.fi/handle/10024/167006.

[21] C. Nordling and J. Österman, *Physics Handbook: for Science and Engineering*, English, 9th. Lund, Sweden: Studentlitteratur AB, 2020, ISBN: 978-91-44-12806-1.

[22] R. J. Roark and W. C. Young, *Roark’s Formulas for Stress and Strain*, 6th. New York, NY: McGraw-Hill, 1989, ISBN: 0070725411.

[23] M. Ettorre, R. Sauleau, L. Le Coq, and F. Bodereau, “Single-folded leaky-wave antennas for automotive radars at 77 ghz,” *IEEE Antennas and Wireless Propagation Letters*, vol. 9, pp. 859–862, 2010. DOI: 10.1109/LAWP.2010.2071850.

DEPARTMENT OF ELECTRICAL ENGINEERING
CHALMERS UNIVERSITY OF TECHNOLOGY
Gothenburg, Sweden
www.chalmers.se

CHALMERS
UNIVERSITY OF TECHNOLOGY